ELISA: A Tool for Optimization of Rotor Hover Performance at Low Reynolds Number in the Mars Atmosphere


Witold J. F. Koning* — *Aerospace Engineer*
B. Natalia Perez Perez — *Aerospace Engineer*
Science & Technology Corporation, NASA Ames Research Center
Moffett Field, California 94035



Haley V. Cummings — *Aerospace Engineer*
Ethan A. Romander — *Aerospace Engineer*
Wayne Johnson — *Aerospace Engineer*
NASA Ames Research Center, Moffett Field, California 94035

The Evolutionary aLgorithm for Iterative Studies of Aeromechanics (ELISA) was developed in support of the Rotorcraft Optimization for the Advancement of Mars eXploration (ROAMX) project. ELISA was developed to enable aerodynamic rotor hover optimization for low Reynolds number flows in the Mars atmosphere. The first module of the algorithm allows for unconventional airfoil parameterization and multiobjective airfoil geometry optimization using OVERFLOW. The Pareto-optimal airfoil sets are converted to a set of Pareto-optimal airfoil decks, providing the lowest drag airfoil geometry for each angle of attack. The second module allows for rotor geometry optimization with simultaneous maximization of blade loading and minimization of rotor power using the comprehensive analysis CAMRADII. The result is a Pareto-optimal rotor set, providing the lowest power rotor for each attainable blade loading, and one of the first tools for hover-optimized rotors for high-subsonic low Reynolds number conditions. The airfoil thickness can be modified after the airfoil optimization is complete, allowing for a post-airfoil optimization adjustment of blade thickness to facilitate conforming to external structural analysis requirements. The relevance of the code is demonstrated with case studies for the ROAMX rotor optimization for Ingenuity-sized single rotors in the Mars atmosphere and a performance study optimizing the chord and twist of Ingenuity's coaxial rotor resulting in the Sample Recovery Helicopters candidate rotor.

Nomenclature

A	rotor disk area, m^2
C_p	pressure coefficient, $(p - p_\infty)/(0.5\rho_\infty U_\infty^2)$
C_P	rotor power coefficient, $P/(\rho_\infty A(\Omega R)^3)$
C_T	rotor thrust coefficient, $T/(\rho_\infty A(\Omega R)^2)$
c	chord, m
c_d	section drag coefficient, $D/(0.5\rho_\infty U_\infty^2 c)$
c_l	section lift coefficient, $L/(0.5\rho_\infty U_\infty^2 c)$
c_m	section pitch moment coefficient, $M_a/(0.5\rho_\infty U_\infty^2 c^2)$
D	section aerodynamic drag force, N/m
f	fitness
FM	rotor hover figure of merit, $T\sqrt{T/(2\rho_\infty A)}/P$
L	section aerodynamic lift force, N/m
L_{Pareto}	Pareto front length
M	Mach number

*Corresponding author; email: witold.koning@nasa.gov
Presented at the VFS 6th Decennial Aeromechanics Specialists' Conference, Santa Clara, CA, February 6–8, 2024. Manuscript received February 2024; accepted July 2024.

M_a	section aerodynamic pitch moment, N
N	number of blades
N_{pop}	population size
P	rotorcraft power, W
R	rotor radius, m; range, km
Re	chord-based Reynolds number, $\rho_\infty U_\infty c/\mu$
r	rotor radial coordinate, m
T	rotor thrust, N; hover time, min
t	airfoil thickness, m
U	velocity, m/s
x	local x coordinate (along chord)
y	local y coordinate (perpendicular to chord)
y^+	dimensionless wall distance
α	angle of attack, deg
μ	dynamic viscosity, Ns/m^2
ρ	density, kg/m^3
σ	thrust-weighted solidity, $\frac{3N}{\pi R}\int_0^R cr^2 dr$
Ω	rotor rotational speed, rad/s

Subscripts

cruise	cruise conditions
d	drag
dd	drag divergence
l	lift
t	thickness
tip	condition at the blade tip
∞	freestream condition
$*$	reference value

Acronyms

CA	comprehensive analysis
ELISA	Evolutionary aLgorithm for Iterative Studies of Aeromechanics
GA	genetic algorithm
LE	leading edge
MOGA	multiobjective genetic algorithm
PO-C81	Pareto-optimal C81
ROAMX	Rotor Optimization for the Advancement of Mars eXploration
SRH	Sample Recovery Helicopter
TE	trailing edge
TRL	technology readiness level
UNS	unsteady Navier–Stokes

Introduction

The Mars helicopter *Ingenuity* made history in April 2021 by being the first aircraft in history to execute powered, controlled flight on another planet (Ref. 1). Before Ingenuity, the high-subsonic low Reynolds number aerodynamics were thought to serve few, if any, practical engineering purposes. Ingenuity's continued success, however, sparked a heightened interest in this aerodynamic regime. While the body of work on rotor aerodynamics at these conditions is still relatively sparse compared to more conventional regimes, it includes notable contributions, including aeromechanical analyses of rotors for Mars conditions at the University of Maryland (Refs. 2–5), experimental progress on airfoil testing at compressible Reynolds numbers at Tohoku University's Mars Wind Tunnel (Refs. 6–11), and computational work for airfoils and rotors at Imperial College London (Refs. 12–14), ONERA and ISAE SUPAERO (Refs. 15,16), Politecnico di Torino (Refs. 17,18), and various other research groups (Refs. 19–21).

Previous work investigated rotor performance predictions for Ingenuity (Refs. 22–24) and explored the possible advantages of cambered plate airfoils as direct substitute to the airfoils present on Ingenuity's rotor. Results showed significant improvements in rotor aerodynamic performance (Ref. 25). Understanding of low Reynolds number aerodynamics was increased by showing the influence of boundary layer transition to small-scale turbulence on rotor performance for a wide range of environmental conditions (Ref. 26). Simulations for an Eppler 387 airfoil showed that the separation, transition, and reattachment of the boundary layer in an unsteady laminar separation bubble are not governed by small-scale transition up to around $Re = 300,000$ in low freestream turbulence (Ref. 27). These findings led future Ingenuity predictions to use laminar unsteady Navier–Stokes (UNS) equations to solve for the aerodynamic flowfield at these conditions (Ref. 24) and led to the insight that the same flow features could then be provoked with unconventional airfoils to potentially improve performance. Optimization of unconventional airfoils was performed and showed that large improvements in aerodynamic sectional performance are possible (Refs. 28,29). Unconventional airfoils were subsequently used in the Mars Science Helicopter concept design to show improvements in rotor performance compared to Ingenuity and demonstrated the structural feasibility of very thin rotor blades to be used in Mars rotor applications (Refs. 5,30). These predictions led to the NASA FY21 Space Technology Mission Directorate Early Career Initiative Project entitled "Rotorcraft Optimization for the Advancement of Mars eXploration" (ROAMX) (Ref. 31). The "Evolutionary aLgorithm for Iterative Studies of Aeromechanics" (ELISA) optimization toolset was developed under ROAMX.

The ROAMX rotor goals will first be discussed, and a high-level overview of the ELISA optimization toolset will be presented. Second, use cases for ELISA are presented: the full ROAMX rotor optimization and the planform and twist optimization for the coaxial sample recovery helicopter (SRH) candidate rotor. Last, concluding remarks and future work will be presented.

ROAMX Rotor Optimization Goals

The ROAMX project aims to find possible increases in rotor performance for an Ingenuity-sized rotor (identical root cutout and radius) by computational optimization and experimental validation of a single rotor in hover, instead of coaxial, to reduce experimental complexity. Furthermore, the objective of ROAMX is primarily to demonstrate isolated hover rotor performance optimization (and not optimization of a vehicle, and antitorque considerations, per se). The sectional airfoil performance is evaluated using OVERFLOW, and the rotor performance is predicted using the comprehensive analysis CAMRADII. Optimizing for rotor hover becomes worthwhile considering the high tip speeds of rotors in the Mars atmosphere and the relatively slow flight speeds of Ingenuity (up to 10 m/s; see Ref. 23), resulting in relatively low advance ratios in forward flight. Rotor optimization for an Ingenuity-sized vehicle in the Mars atmosphere presents several key challenges not yet thoroughly analyzed, compared to studies at higher Reynolds numbers. Optimal airfoils and rotors in the high-subsonic, low Reynolds number regime are still at a low technology readiness level (TRL). Furthermore, efficient approaches to model the high-subsonic, low Reynolds number physics using computational fluid dynamics (CFD), especially with regard to turbulence, transition, and strongly separated flows, are not fully defined. Lastly, optimal rotor shapes and structural analyses of very thin blades at high RPM are complex and can require full three-dimensional (3D) structural analyses

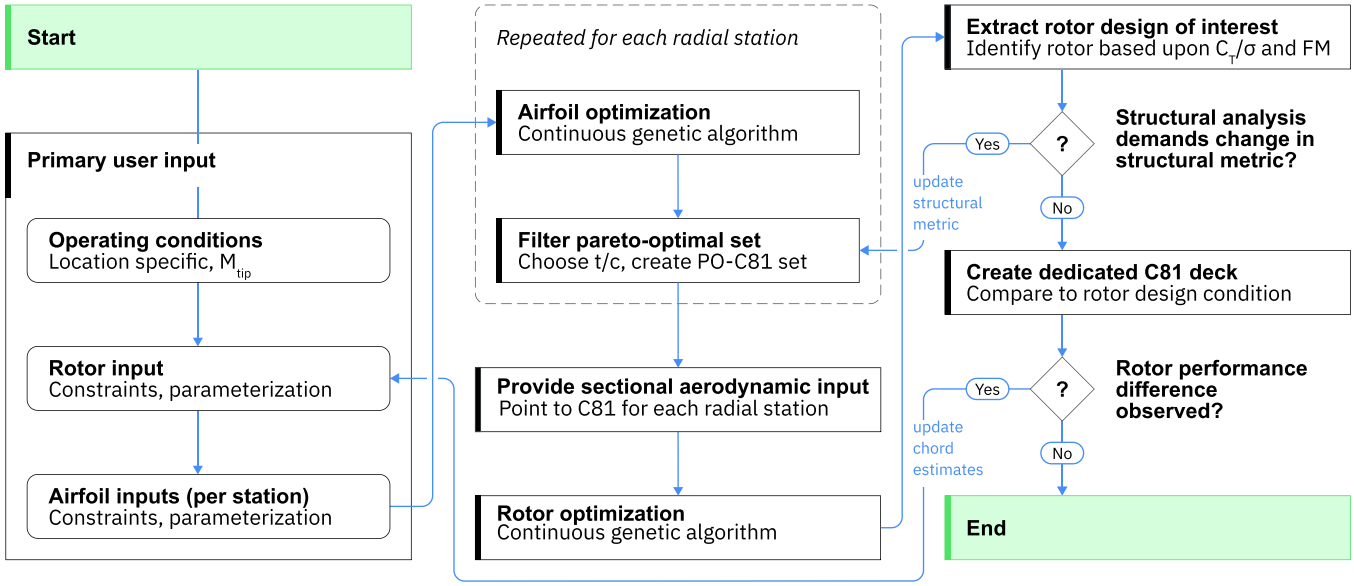

Fig. 1. High-level overview of ELISA optimization toolset.

(compared to using only two-dimensional (2D) sectional properties). These challenges and the lack of a specific mission profile for which to focus the optimization led this project to focus on identifying improvements in possible future rotor performance without predetermined airfoil or rotor design conditions, where possible.

The ELISA Optimization Toolset

The high-level workflow of the ELISA optimization toolset is presented in Fig. 1. Subsequent sections will describe the algorithm, following the main workflow to provide an account of the key components.

Primary user input

The first set of user inputs requires the primary flight conditions for the rotor and includes the tip Mach number, M_{tip}, and location-based conditions (atmospheric density, temperature, dynamic viscosity). As the objective of the code is rotor hover optimization, no trade-offs with cruise speed will be considered and M_{tip} is therefore specified as an input. This avoids optimization up to drag-divergence Mach numbers (and thereby strongly limiting any forward flight speed, M_{cruise}). The tip Mach number is partially estimated by the drag divergence characteristics, M_{dd}, in the aerodynamic regime of interest. In general, it is desired to ensure that $M_{\text{tip}} + M_{\text{cruise}} \ll M_{dd}$. Preliminary numerical and experimental studies have shown that the chosen tip Mach number of $M_{\text{tip}} = 0.80$ has sufficient distance to the Mach divergence number.

User input for the rotor segment includes the rotor radius, rotor root cutout, the radial stations at which airfoil optimization is to be performed, and the corresponding chord estimates at those radial stations. The chord estimates will lead to the Reynolds number estimates for each airfoil, combined with the operating condition from the previous input block. The rotor chord and twist can both be optimized and are either not parameterized (individual values per radial station), or use a linear, quadratic, or cubic Bézier curve for their parameterization. Radial locations can be chosen at which negative taper and/or twist starts to be enforced further outboard. The rotor optimization has dual objectives: maximization of blade loading, C_T/σ, and simultaneous minimization of rotor power, C_P/σ. A minimum C_T/C_P ratio is set to avoid generating designs at very low lift or in stalled conditions, but low-thrust solutions can be kept in the Pareto-optimal rotor selection procedure if so desired.

The airfoil optimization is performed for each radial station in parallel. The airfoil parameterization can be set to `roamx` (dual objectives: maximization of c_l and minimization of c_d) or `roamx3` (`roamx` objectives and maximization of a structural metric or Reynolds number). The structural properties of the airfoil profiles are computed for each iteration and include profile thickness t/c or $(t/c)^2$, or the profile's second moment of area over the chord line. In the current work only t/c is pursued. If `roamx3` optimization is performed, an upper and lower bounds of the structural metric can be selected to constrain the optimization to useful values of the structural metric. A desired minimum c_l/c_d threshold is set to avoid optimizing for stalled conditions (which are nonphysical in 2D and of limited use), but optionally low c_l values can be included in the Pareto-optimal airfoil selection procedure.

Airfoil optimization: Geometry parameterization

The potential of unconventional airfoils (e.g., thin airfoils with sharp leading edges and/or features) was investigated in prior work (Refs. 25,28,29). To more effectively evaluate unconventional airfoil shapes while keeping the number of decision variables to a minimum, the ROAMX parameterization was developed. Contrary to other approaches, the ROAMX parameterization allows for efficient airfoil parameterization and evaluation at low Reynolds numbers: discontinuities along the airfoil profile can be readily explored, the thickness can be fixed if so desired, and the curve order of the camber or thickness segments can be adjusted in order to limit the number of design variables. Figure 2 shows the notation for an example `roamx3-0312` airfoil parameterization.

For both camber and thickness parameterization, the number of "nodes" can be specified and distributed between the leading edge (LE) and the (TE) of the airfoil. These nodes, starting at the LE, are connected by curves as function of chord until the TE is reached. The lines connecting the nodes are represented by Bézier curves which can be chosen to be of first, second, or third order. For each airfoil, the camber, thickness, and a baseline thickness are combined to yield the final airfoil geometry. The baseline thickness is shown in Fig. 3 and serves as a minimum thickness

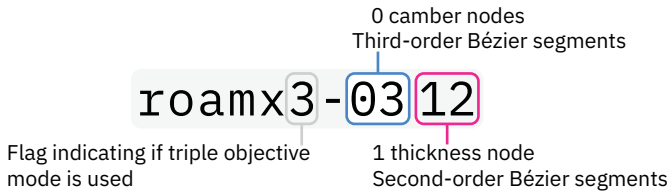

Fig. 2. Notation for ROAMX airfoil parameterization.

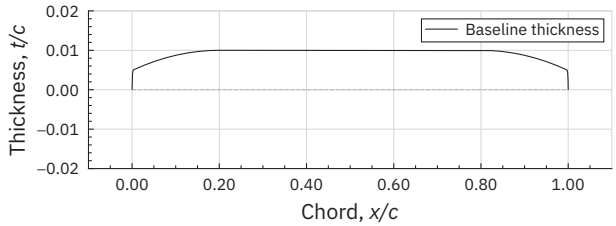

Fig. 3. Baseline thickness distribution.

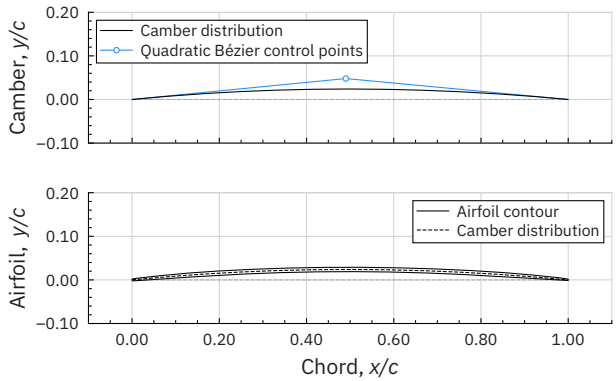

Fig. 4. Example `roamx-0201` parameterization.

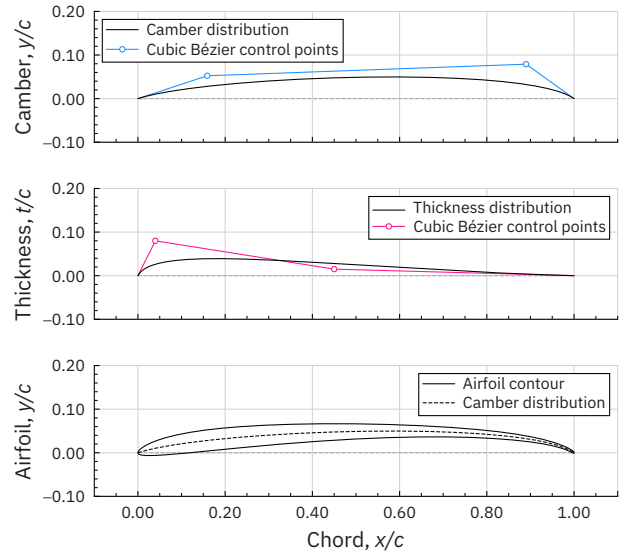

Fig. 5. Example `roamx-0303` parameterization.

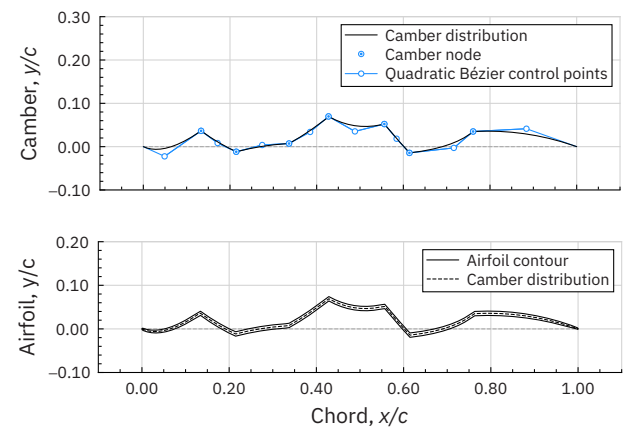

Fig. 6. Example `roamx-7201` parameterization.

constraint (based on manufacturing and/or structural limitations) and is added to the thickness distribution.

The baseline thickness throughout this work is $t/c = 1\%$. The minimum radii at the LE and TE can also be specified to comply with manufacturing constraints.

An example parameterization for a `roamx-0201` airfoil (cambered plate) is shown in Fig. 4. The `roamx-0201` geometry is specified using three decision variables: angle of attack and the two coordinates (x/c), (y/c) of the quadratic Bézier control point. Higher order parameterizations include conventional airfoil geometries within the solution space, as shown in Fig. 5 for a `roamx-0303` parameterization. The `roamx-0303` parameterization has nine decision variables: angle of attack and two pairs of Bézier control points for both thickness and camber.

The primary feature of the ROAMX parameterization scheme allows the user to pick an arbitrary combination of camber and thickness nodes and curve order, allowing for discontinuities along the airfoil profiles so that unconventional profiles can be investigated within the solution space. An example of a dragonfly-like airfoil is shown in Fig. 6, using a `roamx-7201` parameterization.

In contrast to the Bézier control points, the nodes are not allowed to cross each other (i.e., for a node n_i the chordwise location is always constrained so that $x_{n_i} < x_{n_{i+1}}$) and the user can set desired (maximum) slopes to constrain the solution space or to avoid difficulties generating grids for strongly concave corners. The ROAMX parameterization scheme automatically updates all node and control point constraints for thickness and camber during each generation depending on the geometry to result in feasible airfoil geometries that can be reasonably manufactured.

Airfoil optimization: Multiobjective airfoil optimization

The airfoil optimization aims to simultaneously minimize section drag and maximize section lift, resulting in a Pareto-optimal airfoil set. Optionally, the user can specify a third objective which can either be a maximization of a structural metric (the airfoil thickness ratio, t/c, is chosen in the present work) or a Reynolds number.

The optimization is performed by a multiobjective genetic algorithm (MOGA). Compared to gradient-based methods, the advantages of a genetic algorithm (GA) here are the ability to readily evaluate nonsmooth design spaces (problematic computation of a "true mean" for possibly chaotic and unsteady flows in the compressible low Reynolds number regime complicates gradient-based approaches due to nontrivial finite-differencing in these circumstances). Furthermore, the GA allows for relatively straightforward implementation of multiobjective approaches, allowing computation of Pareto-optimal airfoil and rotor sets as

function of airfoil lift, drag, and thickness, and rotor thrust and power, respectively. Finally, the reduced importance of an adequate initial guess close to the global optimum due to the GA's robustness to a domain with several local minimum solutions (of importance here since optimal airfoil and rotor geometries are simply not known) favors a GA approach.

A GA is an iterative heuristic design space search method that starts with a randomly generated set of "individuals" or "chromosomes" (in this case an airfoil represented by its decision variables or "genes"). The set of chromosomes together form the "population" with each iteration of the MOGA, referred to as a generation. The population size for all studies in the present work was set to $N_{\text{pop}} = 20$. Each generation is evaluated using fitness functions that evaluate the degree to which aerodynamic performance targets are met (and section thickness or Reynolds number targets for `roamx3`-type optimizations). Selection of nondominated (Pareto-optimal) individuals to modify and advance the solution to the next generation is done using a bin selection method (Ref. 32), modified here for use for up to three-objective problems as described in the next section. The genetic operators for the MOGA are passthrough (allowing a fit individual to move to the next generation unmodified), random average crossover (averaging all genes of two randomly sampled nondominated individuals), perturbation mutations (user-specified probability of perturbation per gene), and mutations (user-specified probability of complete mutation per gene). More detail on the implementation of these operators and fitness functions is found in Refs. 28 and 32–34. For airfoil optimization, the MOGA computes a Pareto-optimal set which contains the lowest section drag airfoil geometry for each attainable section lift coefficient. If `roamx3`-type problems are solved this set can be readily extracted for each thickness (between user selected lower and upper bounds).

In the present work, the algorithm is terminated after ensuring convergence of the Pareto front length. While the heuristic nature of the MOGA is not well suited for finding the exact global solution quickly, the goal here is to explore shapes that are optimal in this space in general and to advance the understanding and TRL of these airfoils and blades, in the absence of knowing what optimal geometries look like.

Airfoil optimization: Bin selection for triple-objective problems

Evaluation of Pareto-optimality in multiple dimensions readily provides the selection pool for the genetic operators. Less trivial is the selection algorithm in three dimensions. Reference 32 introduces the bin selection algorithm and demonstrates its benefit over classic "tournament" or "greedy" selection procedures. The bin selection algorithm applies to dual objective problems and computes the length between adjacent points along the Pareto front. The selection procedure then first picks the solutions at the endpoints of the Pareto front and then follows by uniquely sampling the points with the biggest "gaps" in the Pareto front first, until the population size is met. This approach greatly promotes an even distribution along the Pareto front. Furthermore, if an individual is found with a relatively large fitness improvement compared to its neighbors, this procedure equivalently ensures that the fit individual is sampled more frequently due to its distance to its neighbor, propagating the genetic information more frequently as long as the relative advantage (i.e., gap) prevails. This method is used for dual objective problems with 2D Pareto optimal sets. Figure 7 shows an example 3D Pareto front based on fitness values for lift, drag, and thickness.

The fitness values for lift, drag, and thickness are described by

$$f_l = \left(1 - \frac{c_l}{c_l^*}\right)^2 \quad f_d = \left(1 - \frac{c_d^*}{c_d}\right)^2 \quad f_t = \left(1 - \frac{t/c}{t^*}\right)^2,$$

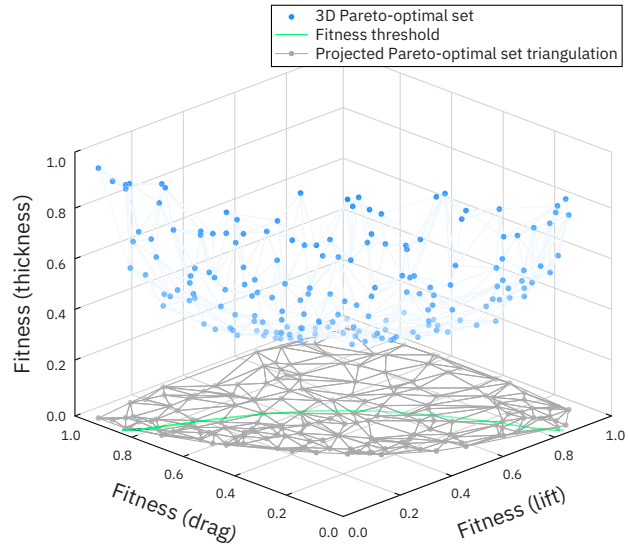

Fig. 7. Example 3D Pareto-optimal set.

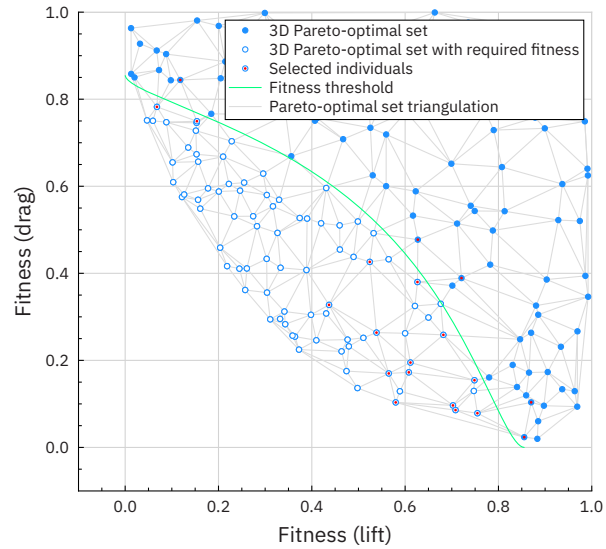

Fig. 8. Selection procedure in 3D projected onto the 2D lift and drag plane.

where c_l^*, c_d^*, and t^* are (unattainable) reference values (Ref. 28). Due to the nature of Pareto-optimality, one can interpret this front as "shell"-like shape, indicated by the Pareto-optimal markers. This therefore allows for computation of the relative separation of the Pareto-optimal cases and their neighbors along the front.

In the ELISA optimization toolset, the bin selection procedure is expanded to allow computation of distance to neighbors in three dimensions. A triangulation is performed on the 3D dataset to create a 3D surface. For clarity, the 2D projection of the triangulation onto the lift and drag plane is shown in Fig. 8.

The Pareto-optimal set is reduced to triangles that have at least one of their vertices within the aerodynamic performance threshold (c_l/c_d ratio) and within the lower and upper thickness thresholds. The dataset is now used to compute the area of the 3D triangles. Ordering the triangles by area (large to small) and listing unique nodes allows for the selection of individuals in three-objective space until the population size is met.

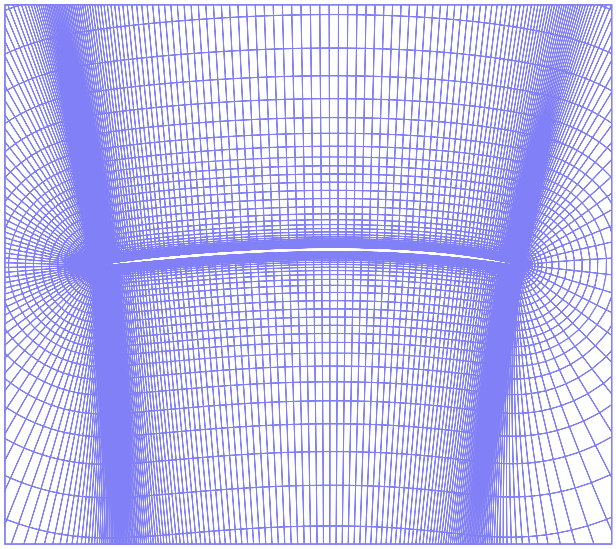

Fig. 9. Example `roamx-0201` near-body grid (every other grid point skipped for clarity).

Airfoil optimization: Function evaluation in OVERFLOW

All airfoil performance function evaluations are performed using 2D CFD with structured overset grids and solved using the implicit, compressible Navier–Stokes solver OVERFLOW 2.3d (Refs. 35,36). Inviscid fluxes are computed using the HLLE++ flux schemes with a fifth-order WENOM upwind reconstruction approach for high spatial accuracy with low numerical dissipation (Ref. 37). Viscous fluxes are computed using second-order central differencing, as are grid metric terms. Time advance uses a second-order backward differencing scheme, with a dual time-stepping approach as described in Refs. 38 and 39.

The user can provide the inputs for the airfoil optimization to provide full flexibility to adjust the simulations for the aerodynamic regime of interest. All analyses presented in this work are performed using laminar UNS equations, and no turbulence model is employed (as discussed in the following paragraphs). This approach attempts to resolve the flow down to the grid resolution, leaving scales below the grid level (in time or space) unevaluated. Simulations in the present work are set up using a set of coarse timesteps at first to remove the initial transients before starting the time-accurate runs. During postprocessing, the transients of the time-accurate part of the simulations are evaluated to remove them from the computation of the mean and compute the corresponding confidence intervals (according to Ref. 40).

The location of the LE, nodes, and TE is provided to the grid generation script which automatically refines the chordwise spacing around discontinuities in the grid. The basic grid generation of the airfoils is described in Refs. 24 and 27, but the maximum chordwise and off-body separation was set at $1\%c$ to reduce the grid size and computation time. The dimensionless wall distance is kept below $y^+ = 1$ for all cases. Grid dimensions vary between different analyses presented in this work, but the grid dimensions are on the order of 1000 chordwise and 250 normal grid points. A representative part of the near-body grid for a `roamx-0201` parameterized airfoil is presented in Fig. 9.

The hypothesis motivating the numerical approach taken herein is that the smaller scales, while existing, do not contribute meaningfully to the mean forces on the airfoils in the compressible, low Reynolds number regime. This was substantiated by previous work showing satisfactory correlation up to relatively high Reynolds numbers ($Re < 300,000$) for Eppler 387 airfoil performance using laminar UNS at low Reynolds numbers ($60,000 \leq Re \leq 460,000$) in the experimental data (Ref. 27). The study showed that mean behavior of unsteady laminar separation bubbles can be captured accurately using laminar UNS and transition to turbulence was governed by a separated shear layer instability resulting in the shedding of large-scale coherent vortices, resulting in reattachment of the mean flow only. Similar shear layer instabilities are observed in the sectional simulations for the Ingenuity rotor performance model (Refs. 23,24) alluding to similar mechanisms at play, and the relative importance of large-scale coherent motion when compared to small-scale turbulence.

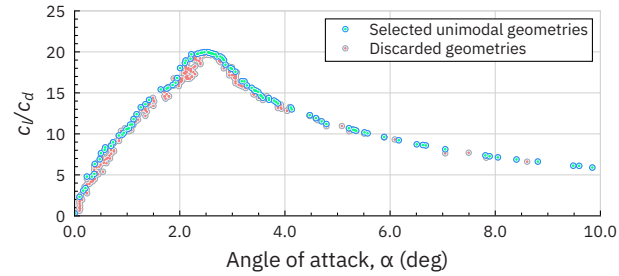

Fig. 10. Lift-to-drag ratio filtering of the Pareto-optimal airfoil set ($Re = 28,058$, $M = 0.80$).

The study also showed that the primary instability mechanism is 2D as separation-reattachment locations are also predicted with reasonable accuracy when evaluating strictly 2D simulations. In the absence of validation data at Mars conditions for unconventional airfoils, this is used as partial justification for the use of 2D simulations instead of 3D simulations in the present work.

The airfoil function evaluation is the constraining element of the ELISA workflow. The airfoil optimization code automatically distributes each chromosome to a dedicated node on the Pleiades Supercomputer at NASA Ames Research Center to compute the whole generational fitness in parallel to efficiently advance the solutions. For the examples provided in this work, the average solution advance required approximately 45 min of wall time per generation and the majority of the Pareto-fronts are well-defined after around 50–100 generations with a population size of $N_{\text{pop}} = 20$.

Pareto-optimal C81 deck filtering

"C81 decks" are a specific format of text files of airfoil lift, drag, and moment coefficients, as a function of angle of attack and Mach number (C81 was an early rotorcraft comprehensive analysis program, for which the format was defined). Once airfoil optimization is completed, the Pareto-optimal sets are filtered to generate the Pareto-optimal C81 (PO-C81) decks. If a `roamx3`-type optimization is pursued, the 3D Pareto-optimal set (function of c_l, c_d, t/c) is first used to extract a 2D Pareto optimal set (function of c_l, c_d) by evaluating Pareto-optimality subjected to the desired thickness constraint. The 2D Pareto-optimal airfoil set (the set of airfoils representing the lowest section drag geometry for each attainable section lift) is now arranged as section lift-to-drag ratio versus angle of attack (a decision variable for all airfoil optimizations), as shown in Fig. 10.

The distribution represents the Pareto-optimal set, and as such reflects a family of airfoils. Next, lower efficiency individuals are discarded by enforcing a strict unimodal (i.e., having only a single highest value) lift-to-drag ratio distribution with angle of attack. Any duplicate angles of attack (down to two decimal places) are removed here to avoid ambiguity since angle of attack is used to trace back the airfoil geometries in the

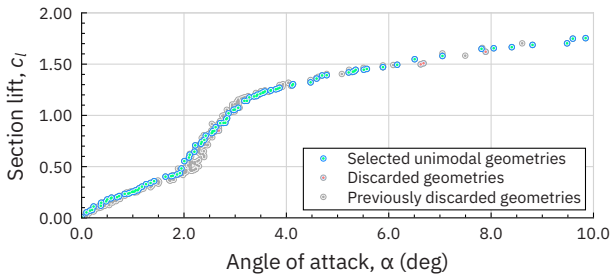

Fig. 11. Lift-filtering of the reduced Pareto-optimal airfoil set.

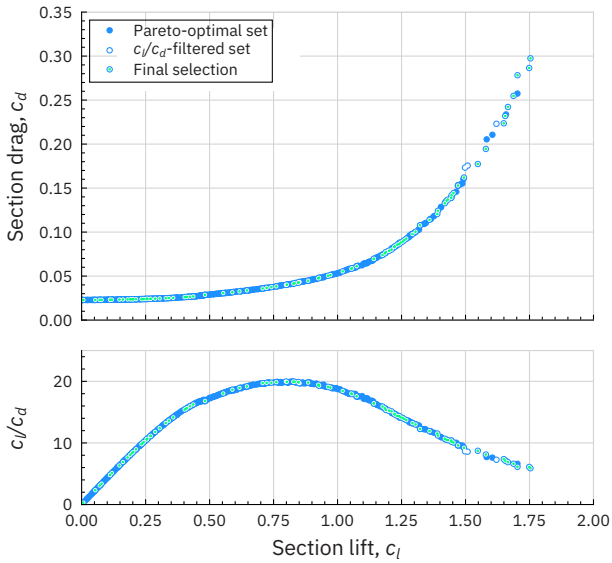

Fig. 12. Final filtering of Pareto-optimal airfoil set.

rotor optimization phase. The reduced Pareto-optimal set is now ordered as section lift versus angle of attack, as shown in Fig. 11.

The filter now discards lower lift individuals by enforcing a strict unimodal section lift distribution with angle of attack. The final Pareto-optimal set is now shown in Fig. 12.

For angles of attack outside of the optimization range, experimental section data for a NACA 0012 profile is automatically added to the set to facilitate the rotor optimization stability. The selection of the Pareto-optimal airfoil set is now finally reduced if the set contains more than the allowable 99 angle of attack entries in a C81 deck. Reduction is implemented by eliminating individuals that are closest to their nearest neighbors in terms of angle of attack.

As the filtered Pareto-optimal set now has an unimodal section lift with respect to angle of attack while keeping the most efficient geometries, the set can now be formatted into proper PO-C81 decks for each radial station. CAMRADII will query the C81 table for performance based on input Mach and angle of attack. Afterward, it will retrieve the section airfoil coefficients for that particular condition—resulting in geometry for the lowest possible drag corresponding to the lift of that entry.

The airfoil geometry is now tied to the angle of attack as CAMRADII, based on lifting line theory, has no particular notion of airfoil geometry.

Rotor optimization

The rotor optimization is performed using a MOGA, mirroring the approach taken in airfoil optimization. The objectives are twofold: to concurrently minimize rotor power (C_P/σ) and maximize blade loading (C_T/σ), ultimately yielding a Pareto-optimal rotor set. The Pareto-optimal set represents the lowest power rotors across all achievable blade loadings.

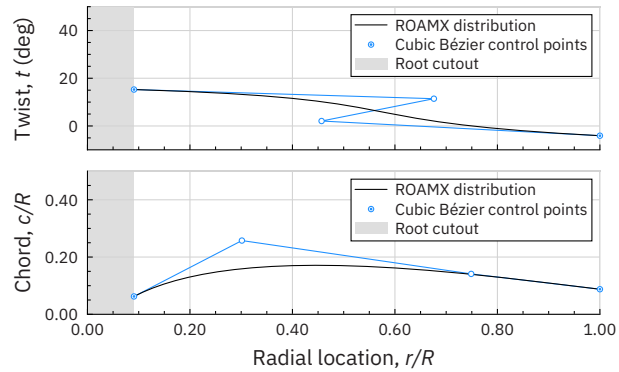

Fig. 13. Example ROAMX rotor parameterization, using cubic Bézier curves for twist and chord.

Rotor optimization: Geometry parameterization

The rotor parameterization closely mirrors the ROAMX airfoil optimization and is designed to parameterize both the twist and planform of the rotor. The same genetic operators are used to modify each generation. The user can specify "no parameterization" (i.e., each chord and twist value is allowed to individually vary) or a linear, quadratic, or cubic Bézier curves may be used to represent the twist and chord. Figure 12 shows an example of twist and chord parameterization using cubic Bézier curves.

The user can set limits to the chord and twist slopes in the outboard region to help converge to realistic rotor geometries. Furthermore, the user can choose to optimize the rotor planform while fixing the thrust-weighted solidity numerically. The root and tip node radial locations are fixed, but the chord and twist values are free (in contrast to the airfoil parameterization where the LE and TE points are fixed). These constraints result in the rotor parameterization in Fig. 13 having 12 decision variables (two pairs of coordinates for the cubic Bézier curves, two root values, and two tip values). The collective is fixed during the optimization, being redundant with twist.

Rotor optimization: Function evaluation in CAMRADII

All rotor performance function evaluations are performed using the Comprehensive Analyses (CA) code CAMRADII (Ref. 41) using nonuniform inflow with a free wake model. The CA model is set up to use the generated PO-C81 tables and predict the corresponding rotor performance. The CAMRADII aerodynamic model for the rotor blade is based on lifting-line theory, using steady 2D airfoil characteristics, a vortex wake model, and additional models for unsteady flow (attached flow and dynamic stall) and yawed/swept flow. Effects of compressibility (Mach numbers) and viscosity (Reynolds number, stall, and drag) enter through airfoil table data: lift, drag, and moment coefficients of 2D sections as function of angle of attack and Mach number, for the appropriate chord and atmosphere (density, temperature) to have the correct Reynolds number variation with Mach number.

Rotor optimization: Dedicated airfoil decks

The rotor optimization results in a Pareto-optimal rotor set from which rotor geometries can be extracted for further analysis. As the

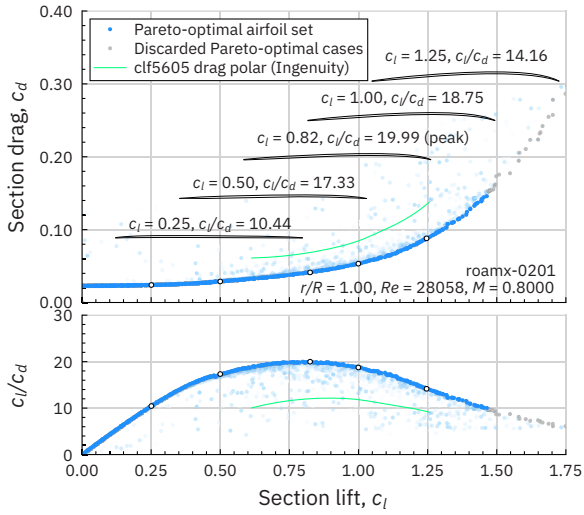

Fig. 14. ROAMX airfoil optimization at $r/R = 1.00$ (dual-objective mode).

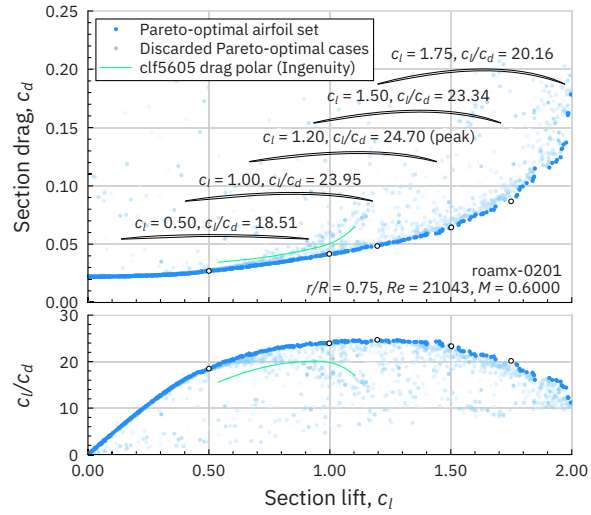

Fig. 15. ROAMX airfoil optimization at $r/R = 0.75$ (dual objective mode).

Reynolds number in the PO-C81 decks (based on the initial chord estimate from the user) can be different from the actual Reynolds number (based on the chord of the optimized rotor planform), there is the possibility for a mismatch in performance between the optimized rotor performance and the actual rotor performance. Furthermore, the angle of attack distribution in the CAMRADII case is used to trace back the airfoil geometries further allowing for discrepancies between the optimization output and the actual rotor performance. This is because CAMRADII will interpolate angles of attack while the PO-C81 decks technically represent discrete airfoils at specific angles of attack.

To verify the optimized rotor performance, a full set of C81 decks for the acquired airfoil and rotor geometries must be generated, to validate that the performance curves include the rotor design blade loading values. As the rotor blade shape is roughly known beforehand (for a particular solidity at least), the requirement to re-iterate the primary ELISA loop was not required for the use cases presented in this work.

ROAMX Rotor Hover Optimization

The first use case for the ELISA optimization toolset is the full rotor hover optimization for the ROAMX project (Ref. 31). The ROAMX project aims to investigate possible isolated rotor performance improvements for the same rotor radius (and root-cutout) as Ingenuity. A single rotor (instead of a coaxial rotor setup) was pursued to facilitate experimental validation in the second phase of the project. The ROAMX rotor optimization is performed for a six-bladed single rotor with a thrust-weighted solidity of $\sigma = 0.25$.

The operating conditions are chosen to be Ingenuity's design operating conditions with a density of $\rho = 0.017$ kg/m^3, commonly referred to as "Mars Condition 2" (Ref. 23). The airfoil optimization is performed at $r/R = 0.0908$, 0.25, 0.50, 0.75, 0.90, and 1.00. The inboard two stations were chosen to have `roamx3`-type optimizations (with variable thickness), and the outboard stations used a total baseline thickness of $t/c = 1\%$. The thin outboard sections allowed for the tip Mach number to be set at $M_{\text{tip}} = 0.80$, while still allowing for 30 m/s forward flight speeds, based on early studies investigating drag divergence behavior for these profiles. Very thin, outboard sections similar to this thickness were shown to be structurally feasible in the Mars Science Helicopter concept design (Refs. 5, 30).

Table 1. Comparison of airfoil performance for $r/R = 1.00$ ($Re = 28{,}058$, $M = 0.80$)

Airfoil	c_l/c_d (Peak)	Relative Change (%)	c_l/c_d ($c_l = 0.91$)[a]	Relative Change (%)
clf5605	12.15	–	12.15	–
`roamx-0201`	19.99	65	19.58	61

[a]Section lift coefficient for clf5605 peak c_l/c_d at this condition.

Airfoil optimization

Figure 14 shows the Pareto-optimal airfoil set for $r/R = 1.00$ (blade tip) conditions, compared to the clf5605 airfoil (used outboard of $r/R = 0.50$ on Ingenuity's rotor 22), evaluated at the same conditions. Figure 15 shows the Pareto-optimal airfoil set for $r/R = 0.75$ conditions compared to the clf5605 airfoil. Both airfoils are parameterized using `roamx-0201` parameterization (quadratic camber variation). The `roamx-0201` parameterization was chosen as it gives a good balance between airfoil performance and number of design variables, other (higher-order) ROAMX parameterizations can yield higher performance (at an increased number of design variables and cost). Both figures show the resulting airfoil geometries for selected section lift coefficients to give an impression of the geometry variation along the Pareto front. The location of the selected airfoils along the Pareto front is indicated using open markers.

The largest airfoil performance improvements are possible at the tip conditions, as the lower thickness and sharp LE combine to delay the critical Mach number and improve low Reynolds number airfoil performance. The minimum lift-to-drag ratio requirement for both sets was set to $c_l/c_d \geq 10$, but the low lift individuals were kept in the Pareto-optimal selection if required in the rotor optimization later.

The peak c_l/c_d for the airfoil optimizations at the tip is compared in Table 1, and the maximum relative change, compared to the clf5605 profile, is around 65%. The relative improvements at $r/R = 0.75$ are lower, but still substantial. The peak c_l/c_d for the airfoil optimizations at $r/R = 0.75$ is compared in Table 2, and the maximum relative change, compared to the clf5605 profile, is around 23%.

To assess the quality of the optimized airfoils in off-design conditions, the polars for a `roamx-0201` optimized airfoil (peak lift-to-drag ratio

Table 2. Comparison of airfoil performance for $r/R = 0.75$ ($Re = 21{,}043$, $M = 0.60$)

Airfoil	c_l/c_d (Peak)	Relative Change (%)	c_l/c_d ($c_l = 0.91$)[a]	Relative Change (%)
clf5605	20.06	–	20.06	–
`roamx-0201`	24.70	23	23.82	19

[a]Section lift coefficient for clf5605 peak c_l/c_d at this condition.

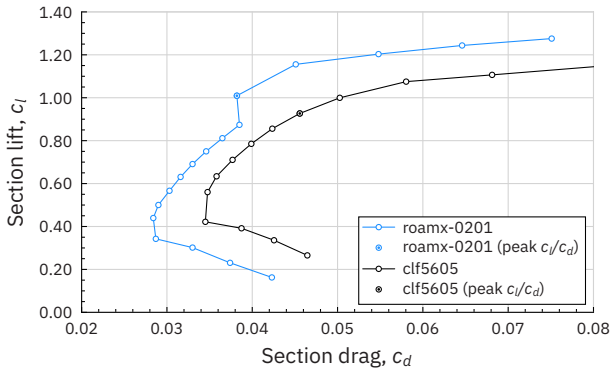

Fig. 16. Comparison of `roamx-0201` and clf5605 airfoil polars.

from the Pareto-optimal airfoil set) and the clf5605 airfoil are compared in Fig. 16. The operating conditions were chosen to reflect those at $r/R = 0.75$ as representative of the aerodynamics over the blade ($Re = 20,000$ and $M = 0.60$).

The inboard sections at $r/R = 0.0908$ and 0.25 were optimized using `roamx3`-type parameterization. This parameterization allowed the Pareto-optimal airfoil sets (as function of lift and drag) to be readily re-evaluated based on structural requirements (here thickness, t/c) as informed by the external structural analysis of the optimized blade (Ref. 4) after the airfoil and rotor optimization were performed.

Figure 17 shows the airfoil optimization using triple-objective mode, highlighting the Pareto-optimal airfoil set for a $t/c \geq 10\%$ requirement.

The minimum lift-to-drag ratio requirement for the sets was $c_l/c_d = 5$, but the low lift individuals were kept. Additional Pareto-optimal sets for $t/c = 4\%$ and 8% are indicated to illustrate the nature of the 3D Pareto-optimal airfoil set.

To present the convergence of the airfoil optimization, the peak lift-to-drag ratio at $r/R = 0.75$ as function of generation, as shown in Fig. 15, is presented in Fig. 18. Figure 18 can, however, present a misleading picture as only singular optimized values are shown, versus a representation of the state of the whole Pareto front. In the absence of knowing the true final value of the optimization problem, one can plot the length of the Pareto front to get an impression of the convergence instead. Figure 19 shows the normalized Pareto front length during the optimization for $c_l/c_d \geq 10$.

Rotor optimization

The rotor optimization was evaluated for a fixed thrust-weighted solidity of $\sigma = 0.25$, for a six-bladed single rotor. The planform and twist distributions were both parameterized using cubic Bézier curves.

The resulting Pareto-optimal rotor set attempts to simultaneously minimize rotor power, while maximizing blade loading and is presented in Fig. 20. Ingenuity performance predictions are presented, modeled as a single four-bladed rotor in CAMRADII (coaxial benefits are removed to present a fairer comparison) at $M_{tip} = 0.80$.

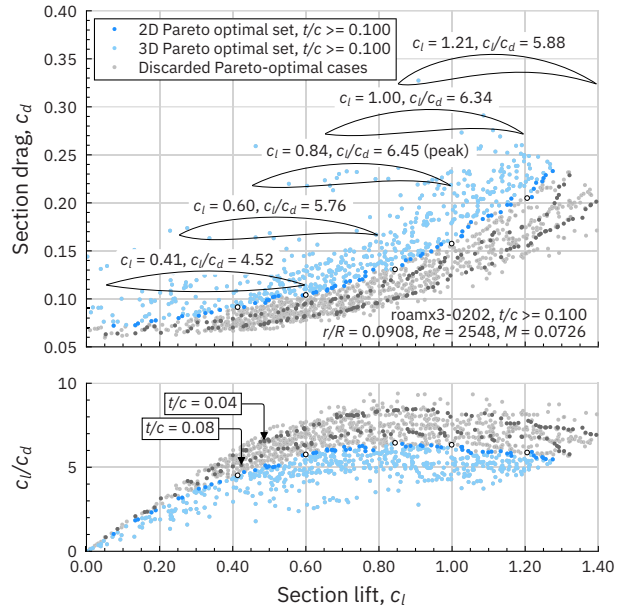

Fig. 17. ROAMX airfoil optimization at $r/R = 0.09$ (triple objective mode), 2D Pareto front for $t/c > 0.10$.

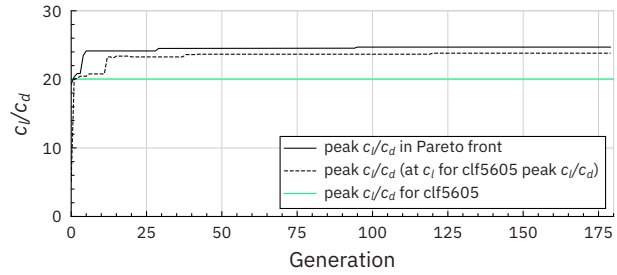

Fig. 18. Convergence of ROAMX airfoil optimization at $r/R = 0.75$.

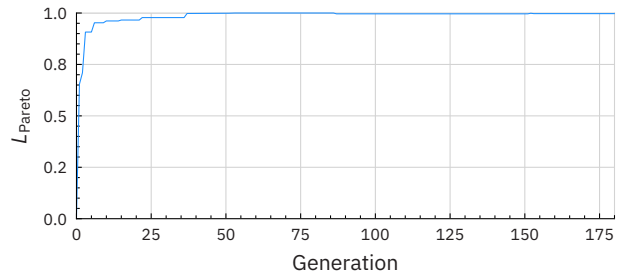

Fig. 19. Pareto-front length for ROAMX airfoil optimization at $r/R = 0.75$.

The Ingenuity design thrust coefficient range is presented as well to identify the primary region of interest. Expressing the dataset as figure of merit versus blade loading highlights the attained differences in rotor efficiencies as shown in Fig. 21.

Three design blade loading targets (at $C_T/\sigma = 0.115$, 0.150, and 0.175) are highlighted in the Pareto-optimal set. By extracting the angle of attack over the blade from the CAMRADII cases, the airfoil geometries were obtained for each radial station and each design blade loading. For those rotor geometries dedicated airfoil decks are generated which are used to validate that the design conditions were met, as shown by the dotted lines. For these airfoil decks, the Reynolds number was updated based on the possible change in chord from the optimized planforms.

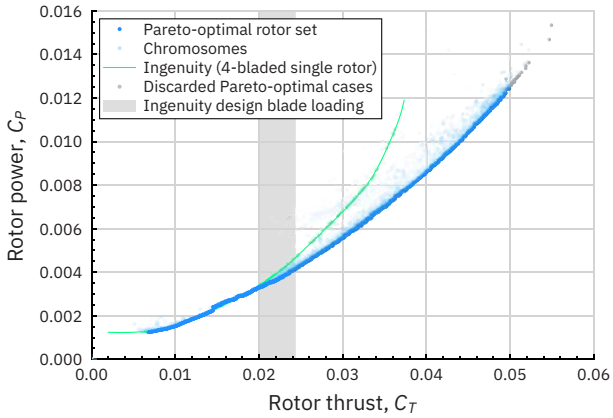

Fig. 20. Pareto-optimal rotor set for the ROAMX rotor.

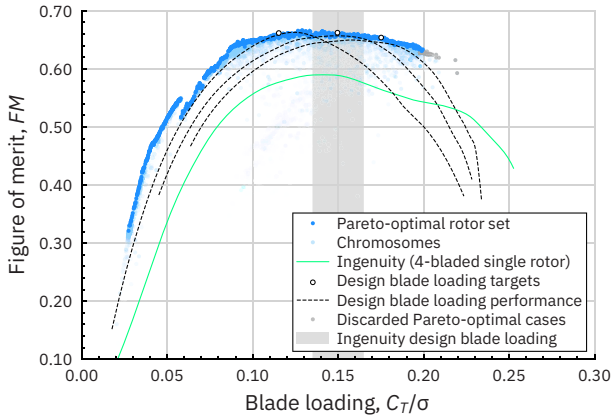

Fig. 21. Pareto-optimal rotor set for the ROAMX rotor, including thrust sweeps for three design points of interest.

Table 3. Comparison of ROAMX rotors to Ingenuity

Rotor Geometry	Figure of Merit (*FM*)	Relative Change (%)[a]
Ingenuity (four-bladed single rotor, $C_T/\sigma = 0.115$)	0.56	–
ROAMX $C_T/\sigma = 0.115$	0.66	19
ROAMX $C_T/\sigma = 0.150$	0.66	12
ROAMX $C_T/\sigma = 0.175$	0.65	15

[a]For equal blade loading.

Table 3 shows an overview of the figure of merit changes at the design blade loading conditions, compared to Ingenuity's performance (modeled as a single four-bladed rotor). The highest blade loading design ($C_T/\sigma = 0.175$) was ultimately selected for further investigation in the ROAMX project. The rotor corresponding to this design point will now be called "the ROAMX rotor."

Since the optimization results in single design points, verifying that the rotor is not "too optimized" and still has a useful thrust margin beyond its design condition is a valuable exercise. As rotor stall is hard to predict accurately, "thrust margin" is interpreted here as a possible 50% increase in blade loading without reduction of the figure of merit. The rotor hover efficiency for the $C_T/\sigma = 0.175$ rotor design is then $FM = 0.64$ for an effective design blade loading of $C_T/\sigma = 0.125$.

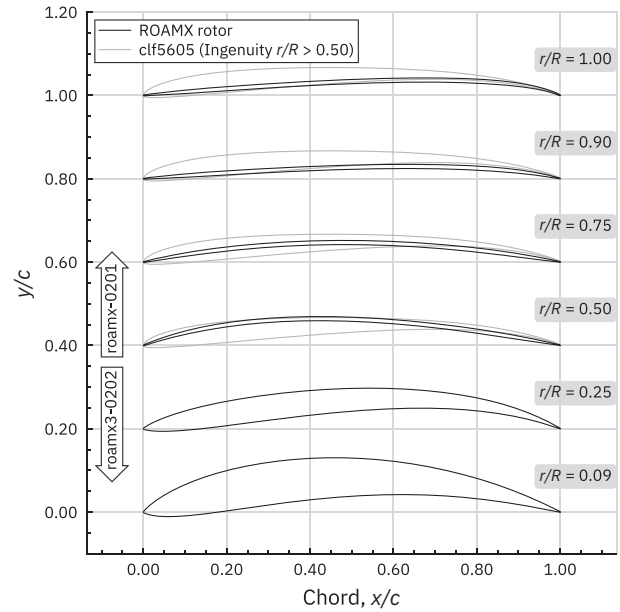

Fig. 22. ROAMX rotor ($C_T/\sigma = 0.175$) airfoils compared to Ingenuity outboard.

Figure 22 shows the airfoils for the $C_T/\sigma = 0.175$ ROAMX rotor and compares them in the outboard region to the Ingenuity clf5605 profiles.

Figure 23 shows the optimized rotor twist and chord distributions for the ROAMX rotor at $C_T/\sigma = 0.175$. The twist and chord distributions for Ingenuity are plotted for reference, as are the cubic Bézier control points for this optimization.

Full rotating blade structural analysis and design of the carbon-fiber ply layup of the ROAMX blade have been performed in Ref. 4 as shown in Fig. 24. The analysis shows that the blade is safe for all testing conditions with a safety factor of two (up to $M_{\text{tip}} = 0.95$). The pitch axis was moved to 40% of the chord to significantly reduce blade root loads and 3D stresses.

Despite the low blade thickness and the risk of significant deformation under load, no adjustments of the blade twist were performed to attain predicted performance with a flexible blade analysis. Aerodynamic loads are low (around 1% of the inertial loads) so that the inertial forces are the primary source of stresses in the blade in hover. This warrants decoupling of the aerodynamic and structural analyses as performed in this study to a degree. Despite these points, manufacturing such a blade remains a limitation of the study and warrants further analysis.

The blade has been manufactured, as shown in Fig. 25. To accommodate the diameter of the ROAMX hub, the rotor radius was scaled up to $R = 720$ mm, and the root cutout was increased to allow for a larger motor for testing during the ROAMX project. The adjusted root geometry is labeled in Fig. 23 as "final".

Improvements in rotor performance can trickle down into the vehicle design. An increase in figure of merit can, for example, reduce the required power, and hence require smaller motors, and batteries, resulting in less required thrust, etc. For an Ingenuity-sized vehicle, the impact of the ROAMX rotor on vehicle performance is computed and shown in Fig. 26, and compared to early airfoil optimization results (Refs. 28, 30) and Ingenuity's rotor performance model (Refs. 23, 24) at $M_{\text{tip}} = 0.80$.

Blade thickness study

To investigate the influence of the blade thickness on ROAMX rotor performance improvements, a study was performed with triple-objective

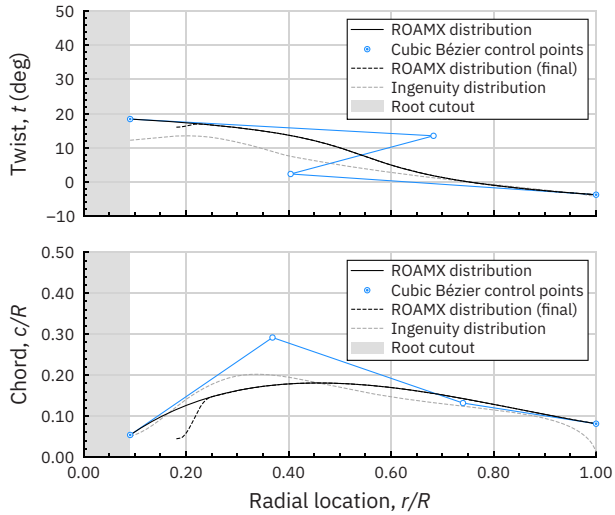

Fig. 23. ROAMX rotor planform and twist, compared to Ingenuity.

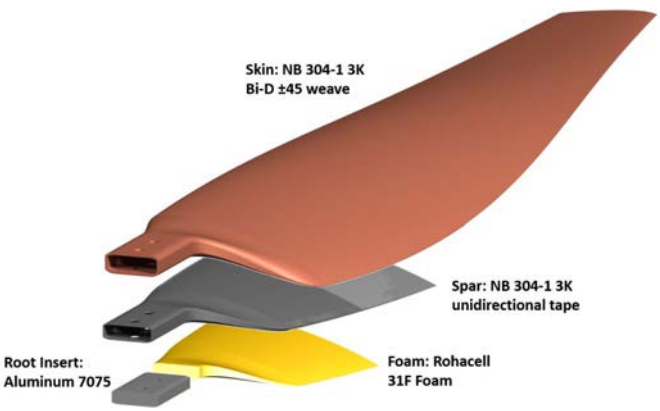

Fig. 24. Materials and internal structure of the ROAMX blade (from Ref. 4).

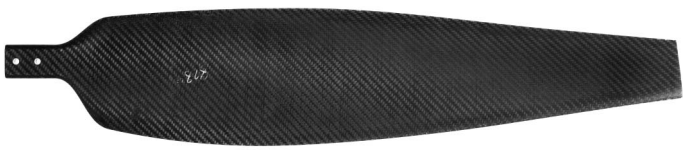

Fig. 25. Manufactured ROAMX blade.

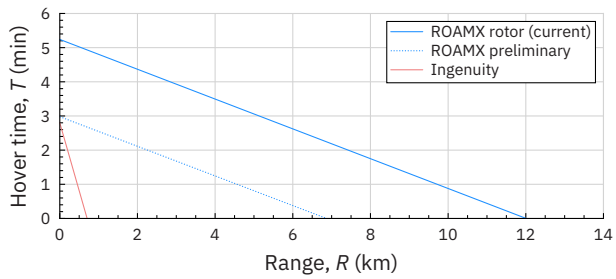

Fig. 26. Hover time versus range estimates for an Ingenuity-sized vehicle with various rotors.

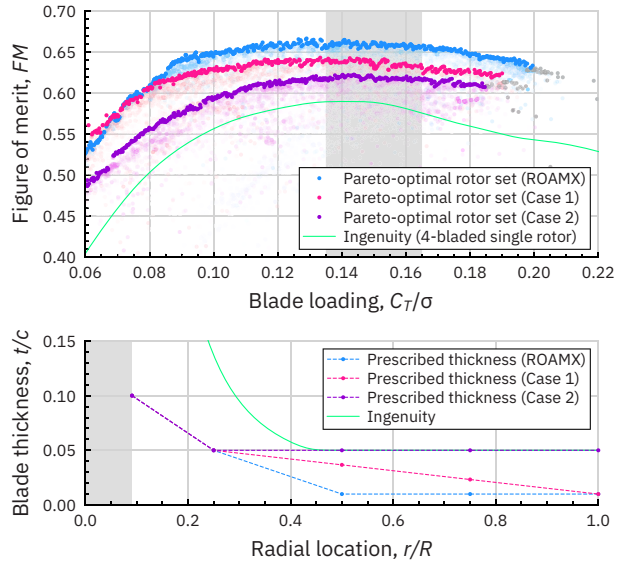

Fig. 27. The influence of blade thickness profiles on Pareto-optimal rotor sets.

airfoil optimizations (`roamx3-0202` parameterization) for $r/R = 0.0908$, 0.25, 0.50, 0.75, and 1.00. Rotor optimization was subsequently performed for two different blade thickness distributions: minimum $t/c = 5\%$ throughout (Case 2), and linear thickness reduction to $t/c = 1\%$ from $r/R = 0.25$ outboard (Case 1). Expressing the dataset as figure of merit versus blade loading highlights the attained differences in rotor efficiencies, as shown in Fig. 27.

The Pareto-optimal rotor sets show the clear influence of the thickness on attainable rotor figure of merit values. However, Fig. 27 also shows that even at a constant $t/c = 5\%$ outboard (Case 2), improvements are still achievable with different rotor geometry and airfoils.

The rotor geometry for $C_T/\sigma = 0.175$ is extracted for the Case 2 thickness profile. Figure 28 shows the airfoils for the `roamx3-0202` parameterization and the Case 2 thickness profile (as shown in Fig. 27). The ROAMX rotor airfoil profiles in Fig. 22 are shown for comparison.

Sample Recovery Helicopter Coaxial Rotor Optimization

Recently, the SRH element was announced in Ref. 42, serving as the primary backup for soil sample tube retrieval as part of the Mars Sample Return (MSR) Campaign.[1] The MSR program aims to bring Mars materials back to Earth for the first time. Under current planning, a ample Retrieval Lander will bring a small rocket, the Mars Launch System, and two SRHs to Mars in 2030. The SRH mission leverages the design heritage of Ingenuity: each helicopter consists of an Ingenuity-like rotorcraft with the addition of ground mobility and a manipulator. An experimental validation campaign to explore higher thrust from an Ingenuity-like rotor was performed by the Jet Propulsion Laboratory with support from AeroVironment, Inc. (Refs. 24, 42). The SRH mission element leverages the technical capabilities demonstrated by Ingenuity. The increased mass of the vehicle (due to the ground mobility and manipulator) requires increased rotor thrust and power, reducing control and power margins. The ELISA optimization toolset was used to optimize the Ingenuity coaxial rotor hover performance, while keeping the heritage airfoils (Ref. 22)

[1]The decision to implement Mars Sample Return will not be finalized until NASA's completion of the National Environmental Policy Act (NEPA) process. This document is being made available for information purposes only.

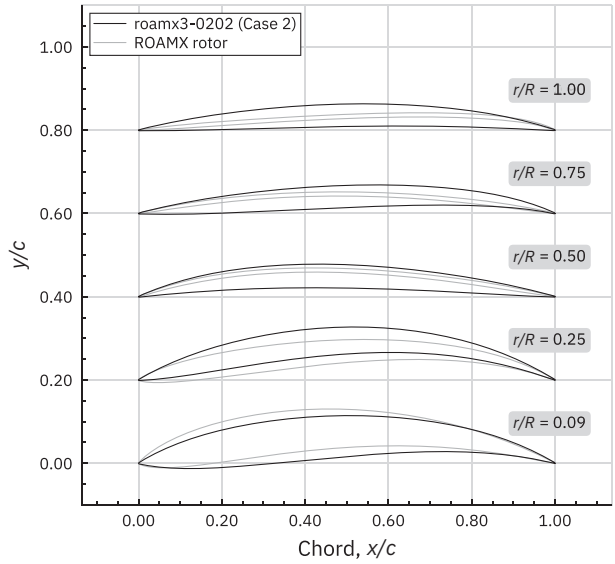

Fig. 28. Example airfoil geometries for `roamx3-0202` airfoil optimization at $C_T/\sigma = 0.175$, compared to the ROAMX rotor.

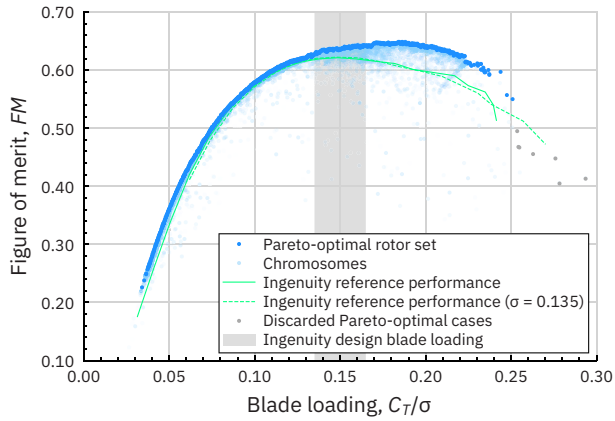

Fig. 29. Coaxial optimization of planform and twist for $\sigma = 0.135$.

along the blade. Several thrust-weighted solidities of $\sigma = 0.135$, 0.150, 0.180, and 0.210 were investigated to identify possible performance improvements.

Rotor optimization

The airfoils are not optimized for this study, and conventional C81 decks are used for the performance predictions. All rotor performance function evaluations are performed using the CA code CAMRADII (Ref. 41) using nonuniform inflow with a free wake model. Variation of angle of attack with azimuth is not a concern as the airfoil geometry now does not vary with angle of attack and the coaxial performance can be readily evaluated. Blade twist and planform were both parameterized using cubic Bézier curves. The Pareto-optimal rotor set for $\sigma = 0.135$ is shown in Fig. 29.

Of the available solidities, the $\sigma = 0.150$ Pareto-optimal rotor set ultimately was studied in greater detail. Figure 30 shows the Pareto-optimal rotor set for figure of merit as function of blade loading, including the collective sweep for the candidate rotor geometry.

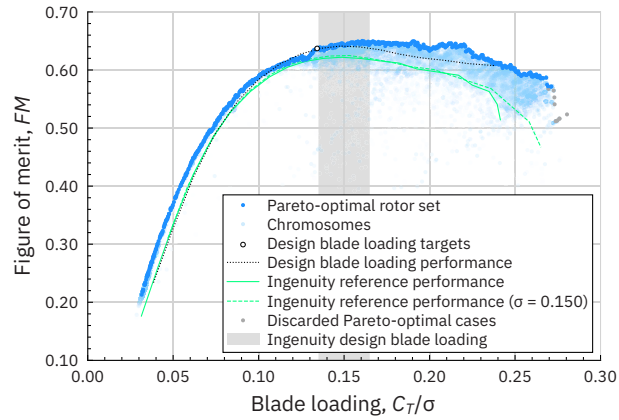

Fig. 30. Coaxial optimization of planform and twist for $\sigma = 0.150$.

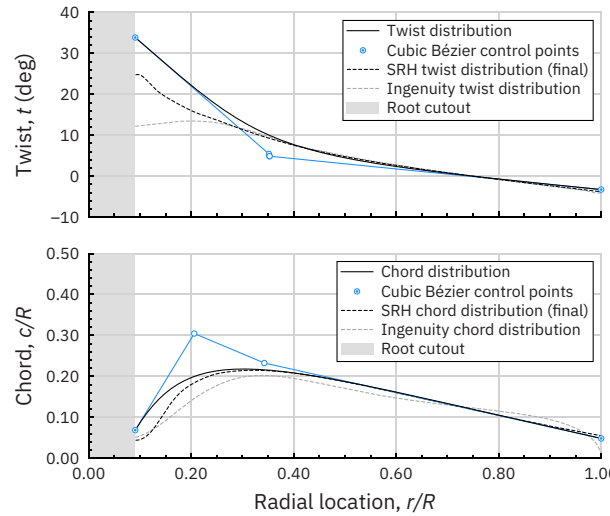

Fig. 31. SRH risk-reduction rotor planform and twist, compared to Ingenuity.

The optimization resulted in an SRH risk-reduction rotor design. Figure 31 shows the twist and chord distributions for this design condition and compares them to the Ingenuity distributions. The outboard twist distribution is virtually unchanged from Ingenuity, but the chord distribution shows a different trend, most notably near the blade tip. The blade geometry was analyzed for structural properties, manufacturability, and integration by AeroVironment, Inc., who also modified the root geometry to arrive at the "final" risk-reduction blade twist and planform distributions.

Optimizations were performed using identical upper and lower blades, as well as a separate optimization allowing for different upper and lower blades. No significant differences were observed for the latter approach, so in favor of the smaller design space, the identical blades were ultimately studied in more detail.

Concluding Remarks and Future Work

The main conclusions and future work for this effort are presented here.

1) The ELISA was developed in support of the ROAMX project.

2) The ELISA optimization toolset was described, introducing the ROAMX airfoil parameterization scheme, Pareto-optimal C81 deck

(PO-C81) generation, postairfoil optimization of the blade, and integration with rotating blade structural analyses.

3) Full optimization of the ROAMX rotor was presented and demonstrated possible increases in peak figure of merit of up to 19% over Ingenuity.

4) A coaxial rotor optimization was performed for Ingenuity's heritage airfoils, to modify the twist and planform to allow for increased performance. The optimization resulted in the SRH risk-reduction rotor design.

Experimental testing has been performed at the Tohoku University Mars Wind Tunnel, Japan, for the clf5605 and `roamx-0201` airfoil. The operating conditions were chosen to reflect those at $r/R = 0.75$ as representative of the aerodynamics over the blade ($Re = 20,000$ and $M = 0.60$). The experimental data will be used to further investigate the performance of these airfoils and compare them to CFD analyses in OVERFLOW. Further collaboration is being set up with Imperial College London to allow their Direct Numerical Simulations using PyFR (Refs. 12–14) to complement the analyses and provide full insight into the aerodynamic behavior of these airfoils at compressible low Reynolds number conditions.

Early studies showed that relative sectional performance improvements are valid in 3D environments. More analysis will need to be performed to evaluate the airfoil performance in 3D environments, both for the airfoil performance (as an extruded 2D profile) as well as the impact of their usage on a practical rotor blade with spanwise variation of airfoils and planform. Similarly, the evaluation of potential shocks near the blade tip, and the implications of evaluation sectional performance versus true 3D environments deserves further attention. High-fidelity 3D CFD simulations are required to explore the detailed aerodynamics and test data are needed to validate the CAMRADII and 3D CFD rotor performance predictions.

ELISA has numerous possible efficiency improvements that can be studied and developed, including improvements in convergence by utilizing an adaptive GA that alters the MOGA hyperparameters (genetic operator probabilities, gene (per)mutation probabilities) as function of generation. Tuning of MOGA hyperparameters for the rotor optimization segment will be studied to improve convergence statistics.

Future work will also expand on airfoil optimization with the Reynolds number as a third objective to investigate optimal shapes as function of the Reynolds number and Mach number. This could result in a surrogate model that could replace the airfoil optimization altogether for a wide range of Reynolds numbers. MOGA is particularly well suited to generating surrogate model input—MOGA is effective in searching 3D space, compared to running a predefined matrix of cases.

Integration of structural analyses within the ELISA optimization toolset, instead of allowing for iterations of a structural metric, would improve the usefulness of the toolset. When a structural model is implemented within the loop, varying alpha with azimuth, and therefore forward flight optimization, could become possible. Rotor optimization can be evaluated along a mass axis and elastic deformations can be fed back into the rotor optimization.

PARSEC airfoil parameterization is currently being implemented into the code to allow for efficient, strictly conventional airfoil optimization. This, in combination with the significantly reduced computation time of airfoil performance at higher Reynolds numbers could allow the ELISA optimization toolset to be used for higher Reynolds number analyses.

The rotor optimizations are primarily aimed at demonstrating the feasibility and performance of unconventional airfoil and rotor optimization and currently represent single-design optima. When a mission profile is identified, a more detailed airfoil design should, at least, consider sufficient margins for lift and Mach number, and rotor optimization should implement a sufficient thrust margin to increase the practical useability of these rotors.

Acknowledgments

Ravi Lumba, Cheng Chi, and Anubhav Datta are thanked for the helpful discussions and their invaluable support in completing this work. The research of Witold J. F. Koning, B. Natalia Perez Perez, and Haley Cummings is made possible by the NASA FY21 Space Technology Mission Directorate Early Career Initiative Project "Rotor Optimization for the Advancement of Mars eXploration." Lidia Caros, Oliver Buxton, and Peter Vincent are thanked for their helpful discussions and expertise. The authors would like to acknowledge the support of William Warmbrodt and Larry Hogle during this research. Tove Ågren, Nicholas Peters, and Sesi Kottapalli are thanked for their feedback in reviewing this paper. Resources supporting this work were provided by the NASA High-End Computing Program through the NASA Advanced Supercomputing Division at Ames Research Center.

References

[1]Balaram, J. (Bob), Canham, T., Duncan, C., Golombek, M., Grip, H. F., Johnson, W., Maki, J., Quon, A., Stern, R., and Zhu, D., "Mars Helicopter Technology Demonstrator," AIAA Paper 2018- 0023, Proceedings of the 2018 AIAA Atmospheric Flight Mechanics Conference, Kissimmee, FL, January 8–12, 2018, DOI: 10.2514/6.2018-0023.

[2]Escobar, D., Chopra, I., and Datta, A., "Aeromechanical Loads on a Mars Coaxial Rotor," Proceedings of the 74th Annual Forum and Technology Display of the American Helicopter Society, Phoenix, AZ, May 14–17, 2018.

[3]Escobar, D., Chopra, I., and Datta, A., "Aeromechanics of a Coaxial Mars Helicopter Using High-Fidelity CFD/CA," Proceedings of the 75th Annual Forum & Technology Display of the Vertical Flight Society, Philadelphia, PA, May 13–16, 2019.

[4]Lumba, R., Chi, C., Datta, A., Koning, W., Perez Perez, N., and Cummings, H., "Structural Design and Aeromechanical Analysis of Unconventional Blades for Future Mars Rotorcraft," *Journal of the American Helicopter Society*, **68**, 42003 (2023), DOI: https://doi.org/10.4050/JAHS.68.042003.

[5]Chi, C., Lumba, R., Su Jung, Y., and Datta, A., "Aeromechanical Analysis of a Next-Generation Mars Hexacopter Rotor," *Journal of Aircraft*, Vol. 59, (6), May 2022, pp. 1463–1477, DOI: 10.2514/1.C036739.

[6]Anyoji, M., Ida, S., Nose, K., Numata, D., Nagai, H., and Asai, K., "Characteristics of the Mars Wind Tunnel at Tohoku University in CO_2 Operation Mode," AIAA Paper 2010-1490, Proceedings of the 48th AIAA Aerospace Sciences Meeting, Orlando, FL, January 4–7, 2010, DOI: 10.2514/6.2010-1490.

[7]Anyoji, M., Nose, K., Ida, S., Numata, D., Nagai, H., and Asai, K., "Low Reynolds Number Airfoil Testing in a Mars Wind Tunnel," AIAA Paper 2010-4627, Proceedings of the 40th Fluid Dynamics Conference and Exhibit, Chicago, IL, June 28–July 1, 2010, DOI: 10.2514/6.2010-4627.

[8]Munday, P. M., Taira, K., Suwa, T., Numata, D., and Asai, K., "Nonlinear Lift on a Triangular Airfoil in Low-Reynolds-Number Compressible Flow," *Journal of Aircraft*, Vol. 52, (3), December 2014, pp. 924–931, DOI: 10.2514/1.C032983.

[9]Anyoji, M., Nose, K., Ida, S., Numata, D., Nagai, H., and Asai, K., "Development of a Low-Density Wind Tunnel for Simulating Martian Atmospheric Flight," *Transactions of the Japan Society for Aeronautical and Space Sciences, Aerospace Technology Japan*, Vol. 9, June 2011, pp. 21–27, DOI: 10.2322/tastj.9.21.

[10]Nagata, T., Sato, H., Okochi, M., Matsuyama, T., Sugioka, Y., Kasai, M., Kusama, K., Numata, D., Nonomura, T., and Asai, K., "Visualization of Pressure and Skin-Friction Fields on Rotating Blade under

Low-Pressure Conditions," *AIAA Journal*, Vol. 60, (9), June 2022, pp. 5422–5435, DOI: 10.2514/1.J061638.

[11]Guilarte Herrero, A., Noguchi, A., Kusama, K., Shigeta, T., Nagata, T., Nonomura, T., and Asai, K., "Effects of Compressibility and Reynolds Number on the Aerodynamics of a Simplified Corrugated Airfoil," *Experiments in Fluids,* **62**, 63 (2021), DOI: 10.1007/s00348-021-03164-0.

[12]Caros, L., Blank, J., Buxton, O., and Vincent, P., "Comparing Strategies for DNS Based Optimization of Airfoils for Martian Rotorcraft," Proceedings of the 78th Annual Forum & Technology Display of the Vertical Flight Society, Fort Worth, TX, May 10–12, 2022.

[13]Caros, L., Buxton, O., Shigeta, T., Nagata, T., Nonomura, T., Asai, K., and Vincent, P., "Direct Numerical Simulation of Flow over a Triangular Airfoil under Martian Conditions," *AIAA Journal*, Vol. 60, (7), March 2022, pp. 3961–3972, DOI: 10.2514/1.J061454.

[14]Caros, L., Buxton, O., and Vincent, P., "Optimization of Triangular Airfoils for Martian Helicopters Using Direct Numerical Simulations," *AIAA Journal*, Vol. 61, (11), August 2023, pp. 4935–4945, DOI: 10.2514/1.J063164.

[15]Désert, T., Moschetta, J., and Bézard, H., "Numerical and Experimental Investigation of an Airfoil Design for a Martian Micro Rotorcraft," *International Journal of Micro Air Vehicles*, Vol. 10, (3), September 2018, pp. 262–272, DOI: 10.1177/1756829318794171.

[16]Désert, T., Jardin, T., Bézard, H., and Moschetta, J., "Numerical Predictions of Low Reynolds Number Compressible Aerodynamics," *Aerospace Science and Technology*, Vol. 92, September 2019, pp. 211–223, DOI: 10.1016/j.ast.2019.05.064.

[17]Carreno Ruiz, M., and D'Ambrosio, D., "Hybrid Fidelity Optimization of Efficient Airfoils and Rotors in Ultra-Low Reynolds Numbers Conditions," AIAA Paper 2023-0652, Proceedings of the AIAA SCITECH 2023 Forum, National Harbor, MD, January 23–27, 2023, DOI: 10.2514/6.2023-0652.

[18]Carreno Ruiz, M., and D'Ambrosio, D., "ROT8: A Matlab App for Low Reynolds Number Airfoil and Rotor Aerodynamic Design," AIAA Paper 2023-3379.c1, Proceedings of the AIAA AVIATION 2023 Forum, San Diego, CA, June 12–16, 2023, DOI: 10.2514/6.2023-3379.c1.

[19]Yoshikawa, K., Buto, Y., Sato, M., Oyama, A., Sugiura, M., Tanabe, Y., Kimura, K., Takekawa, K., Kishi, Y., and Kanazaki, M., "Compressibility Effects on Aerodynamic Characteristics and Flow Fields of Mars Helicopter Rotor," AIAA Paper 2023-4000, Proceedings of the AIAA AVIATION 2023 Forum, San Diego, CA, June 12–16, 2023, DOI: 10.2514/6.2023-4000.

[20]Kishi, Y., Kanazaki, M., Sugiura, M., Tanabe, Y., Oyama, A., and Sato, M., "Numerical Analysis on Hovering Performance of Hexacopter 'HAMILTON' for Mars Exploration," AIAA Paper 2022-4039, Proceedings of the AIAA AVIATION 2022 Forum, Chicago, IL, June 27–July 1, 2022, DOI: 10.2514/6.2022-4039.

[21]Yamaguchi, T., and Anyoji, M., "Numerical Study on Low-Reynolds Compressible Flows around Mars Helicopter Rotor Blade Airfoil," *Journal of Flow Control, Measurement & Visualization*, Vol. 11, (2), April 2023, pp. 30–48, DOI: 10.4236/jfcmv.2023.112003.

[22]Koning, W. J. F., Johnson, W., and Allan, B. G. "Generation of Mars Helicopter Rotor Model for Comprehensive Analyses" Proceedings of the Technical Conference on Aeromechanics Designs for Transformative Vertical Flight of the American Helicopter Society, San Francisco, CA, January 16–18, 2018.

[23]Koning, W. J. F., Johnson, W., and Grip, H. F., "Improved Mars Helicopter Aerodynamic Rotor Model for Comprehensive Analyses," *AIAA Journal*, Vol. 57, (9), September 2019, pp. 3969–3979, DOI: 10.2514/1.J058045.

[24]Koning, W. J. F., Allan, B. G., Romander, E. A., and Johnson, W., "Comparing 3D and 2D CFD for Mars Helicopter Ingenuity Rotor Performance Prediction," Proceedings of the 49th European Rotorcraft Forum, Bückeburg, Germany, September 5–7, 2023.

[25]Koning, W. J. F., Romander, E. A., and Johnson, W., "Low Reynolds Number Airfoil Evaluation for the Mars Helicopter Rotor," Proceedings of the 74th Annual Forum & Technology Display of the American Helicopter Society, Phoenix, AZ, May 14–17, 2018.

[26]Argus, F. J., Ament, G. A., and Koning, W. J. F., "The Influence of Laminar-Turbulent Transition on Rotor Performance at Low Reynolds Numbers," Proceedings of the Aeromechanics for Advanced Vertical Flight Technical Meeting of the Vertical Flight Society, San Jose, CA, January 21–23, 2020.

[27]Koning, W. J. F., Romander, E. A., Cummings, H. V., Perez Perez, B. N., and Buning, P. G. "On Improved Understanding of Airfoil Performance Evaluation Methods at Low Reynolds Numbers." *Journal of Aircraft*, Vol. 60, (3), May 2023, pp. 774–788, DOI: 10.2514/1.C037023.

[28]Koning, W. J. F., Romander, E. A., and Johnson, W., "Optimization of Low Reynolds Number Airfoils for Martian Rotor Applications Using an Evolutionary Algorithm," AIAA Paper 2020-0084, Proceedings of the AIAA Scitech 2020 Forum, Orlando, FL, January 6–10, 2020, DOI: 10.2514/6.2020-0084.

[29]Koning, W. J. F., Romander, E. A., and Johnson, W., "Performance Optimization of Plate Airfoils for Martian Rotor Applications Using a Genetic Algorithm," Proceedings of the 45th European Rotorcraft Forum, Warsaw, Poland, September 17–20, 2019.

[30]Johnson, W., Withrow-Maser, S., Young, L., Malpica, C., Koning, W. J. F., Kaung, W., Fehler, M., Tuano, A., Chan, A., Datta, A., Chi, C., Lumba, R., Escobar, D., Balaram, J., Tzanetos, T., and Grip, H. F., "Mars Science Helicopter Conceptual Design," NASA/TM–2020-220485, 2020.

[31]Cummings, H., Perez Perez, B. N., Koning, W. J. F., Johnson, W., Young, L., Haddad, F., Romander, E., Balaram, J., Tzanetos, T., and Bowman, J., "Overview and Introduction of the Rotor Optimization for the Advancement of Mars eXploration (ROAMX) Project," Proceedings of the Aeromechanics for Advanced Vertical Flight Technical Meeting of the Vertical Flight Society, San Jose, CA, January 25–27, 2022.

[32]Holst, T. L., and Pulliam, T. H., "Evaluation of Genetic Algorithm Concepts Using Model Problems. Part 1; Single-Objective Optimization," NASA/TM–2003-0065967, 2003.

[33]Holst, T. L., and Pulliam, T. H., "Evaluation of Genetic Algorithm Concepts Using Model Problems. Part 2: Multi-Objective Optimization," NASA/TM–2003-212813, 2003.

[34]Pulliam, T., Nemec, M., Holst, T., and Zingg, D., "Comparison of Evolutionary (Genetic) Algorithm and Adjoint Methods for Multi-Objective Viscous Airfoil Optimizations," Proceedings of the 41st Aerospace Sciences Meeting and Exhibit, Reno, NV, January 6–9, 2003, DOI: 10.2514/6.2003-298.

[35]Nichols, R. H., and Buning, P. G. "User's Manual for OVERFLOW 2.2." Langley Research Center, Hampton, VA, 2008.

[36]Pulliam, T. H., "High Order Accurate Finite-Difference Methods: As Seen in OVERFLOW." AIAA Paper 2011-3851, Proceedings of the 20th AIAA Computational Fluid Dynamics Conference, Honolulu, HI, June 27–30, 2011, DOI: 10.2514/6.2011-3851.

[37]Tramel, R., Nichols, R., and Buning, P., "Addition of Improved Shock-Capturing Schemes to OVERFLOW 2.1." AIAA Paper 2009-3988, Proceedings of the 19th AIAA Computational Fluid Dynamics, San Antonio, TX, June 22–25, 2009, DOI: 10.2514/6.2009-3988.

[38]Pulliam, T. H. "Time Accuracy and the Use of Implicit Methods." AIAA Paper 1993-3360, Proceedings of the 11th AIAA Computational Fluid Dynamics Conference, Orlando, FL, July 6–9, 1993, DOI: 10.2514/6.1993-3360.

[39]Pandya, S., Venkateswaran, S., and Pulliam, T. H. "Implementation of Preconditioned Dual-Time Procedures in OVERFLOW." AIAA Paper 2003-0072, Proceedings of the 41st Aerospace Sciences Meeting and Exhibit, Reno, NV, January 6–9, 2003, DOI: 10.2514/6.2003-72.

[40]Bergmann, M., Morsbach, C., Ashcroft, G., and Kügeler, E., "Statistical Error Estimation Methods for Engineering-Relevant Quantities from Scale-Resolving Simulations," *Journal of Turbomachinery*, **144**, 031005 (2022), DOI: 10.1115/1.4052402.

[41]Johnson, W. "Rotorcraft Aerodynamics Models for a Comprehensive Analysis." Proceedings of the 54th Annual Forum & Technology Display of the American Helicopter Society, Washington, DC, May 20–22, 1998.

[42]Mier-Hicks, F., Grip, H. F., Kalantari, A., Moreland, S., Pipenberg, B., Keennon, M., Canham, T. K., Pauken, M., Decrossas, E., and Tzanetos, T. "Sample Recovery Helicopter." Proceedings of the 2023 IEEE Aerospace Conference, Big Sky, MT, March 4–11, 2023, DOI: 10.1109/AERO55745.2023.10115951.